Phys. Med. Biol. **56** (2011) 6649–6664 doi:10.1088/0031-9155/56/20/009

# NEMA NU-04-based performance characteristics of the LabPET-8™ small animal PET scanner

**Rameshwar Prasad**[1], **Osman Ratib**[1] **and HabibZaidi**[1,2,3,4]

[1] Division of Nuclear Medicine and Molecular Imaging, Geneva University Hospital, CH-1211 Geneva, Switzerland
[2] Geneva Neuroscience Center, Geneva University, CH-1211 Geneva, Switzerland
[3] Department of Nuclear Medicine and Molecular Imaging, University Medical Center Gronigen, University of Groningen, 9700 RB Groningen, The Netherlands

E-mail: habib.zaidi@hcuge.ch

Received 26 April 2011, in final form 11 August 2011
Published 23 September 2011
Online at stacks.iop.org/PMB/56/6649

**Abstract**

The objective of this study is to characterize the performance of the preclinical avalanche photodiode (APD)-based LabPET-8™ subsystem of the fully integrated trimodality PET/SPECT/CT Triumph™ scanner using the National Electrical Manufacturers Association (NEMA) NU 04–2008 protocol. The characterized performance parameters include the spatial resolution, sensitivity, scatter fraction, counts rate performance and image-quality characteristics. The PET system is fully digital using APD-based detector modules with highly integrated electronics. The detector assembly consists of phoswich pairs of $Lu_{1.9}Y_{0.1}SiO_5$ (LYSO) and $Lu_{0.4}Gd_{1.6}SiO_5$ (LGSO) crystals with dimensions of $2 \times 2 \times 14$ mm$^3$ having 7.5 cm axial and 10 cm transverse field of view (FOV). The spatial resolution and sensitivity were measured using a small $^{22}$Na point source at different positions in the scanner's FOV. The scatter fraction and count rate characteristics were measured using mouse- and rat-sized phantoms fitted with an $^{18}$F line source. The overall imaging capabilities of the scanner were assessed using the NEMA image-quality phantom and laboratory animal studies. The NEMA-based radial and tangential spatial resolution ranged from 1.7 mm at the center of the FOV to 2.59 mm at a radial offset of 2.5 cm and from 1.85 mm at the center of the FOV to 1.76 mm at a radial offset of 2.5 cm, respectively. Iterative reconstruction improved the spatial resolution to 0.84 mm at the center of the FOV. The total absolute system sensitivity is 12.74% for an energy window of 250–650 keV. For the mouse-sized phantom, the peak noise equivalent count rate (NECR) is 183 kcps at 2.07 MBq cc$^{-1}$, whereas the peak true count rate is 320 kcps at 2.5 MBq cc$^{-1}$ with a scatter fraction of 19%. The rat-sized phantom had a scatter fraction of 31%, with a peak NECR of 67 kcps at 0.23 MBq cc$^{-1}$ and a peak true count rate of 186 kcps at 0.27 MBq cc$^{-1}$. The average activity concentration and percentage standard

[4] Author to whom any correspondence should be addressed.

  

deviation were 126.97 kBq ml$^{-1}$ and 7%, respectively. The performance of the LabPET-8$^{TM}$ scanner was characterized based on the NEMA NU 04–2008 standards. The all in all performance demonstrates that the LabPET-8$^{TM}$ system is able to produce high-quality and highly contrasted images in a reasonable time, and as such it is well suited for preclinical molecular imaging-based research.

(Some figures in this article are in colour only in the electronic version)

## 1. Introduction

Positron emission tomography (PET) has become an integral non-invasive molecular imaging modality in biomedical and biological imaging research (Phelps 2000). PET is now a well-established imaging modality which has gained widespread clinical acceptance. Moreover, the importance of PET for preclinical imaging has increased manifold during the last decade owing to the capabilities of this technique for studying cellular and molecular processes associated with disease in living small animal models of disease (Levin and Zaidi 2007). Clinical whole-body PET scanners are not appropriate for this purpose since they do not provide the high resolution and sensitivity required for small laboratory animal studies (Stout and Zaidi 2008). This has spurred the design and development of various prototypes dedicated for small animal PET imaging (Ziemons *et al* 2005, Tai *et al* 2003, Bloomfield *et al* 1995, Lecomte *et al* 1996, Cherry *et al* 1997, Jeavons *et al* 1999, Del Guerra *et al* 1998, Surti *et al* 2003, Rouze *et al* 2004) following the pioneering work in Hammersmith Hospital (London, UK) in collaboration with CTI PET Systems, Inc. (Knoxville, TN, USA) toward the design of the first rodent PET scanner. This work has resulted in the development of numerous research prototypes as well as several commercially available high-resolution preclinical PET systems (Schafers *et al* 2005, Tai *et al* 2005, Wang *et al* 2006, Huisman *et al* 2007, Bao *et al* 2009, Xie *et al* 2005, Bergeron *et al* 2009a, Prasad *et al* 2010).

The Triumph$^{TM}$ PET/SPECT/CT system (GE healthcare Technologies, Waukesha, WI) is a dedicated trimodality preclinical imaging platform. The scanner consists of the fully digital LabPET$^{TM}$ subsystem (Tetrault *et al* 2008, Bergeron *et al* 2009a), cadmium zinc telluride (CZT)-based detectors for the microSPECT subsystem and a high-resolution microCT subsystem. All three subsystems are mounted on the same gantry offering the possibility to configure the multimodality platform in any combination of the three subsystems. The LabPET$^{TM}$ is the first commercially available APD-based small animal PET scanner designed using a parallel, fully digital signal processing of each detector channel (Fontaine *et al* 2009). The scanner exhibits several innovative design features rendering it as a high-resolution and highly sensitive preclinical PET scanner for small animal imaging (Tetrault *et al* 2008, Bergeron *et al* 2009a). As of today, three variants of the LabPET$^{TM}$ are available depending on the axial field of view (FOV), namely LabPET$^{TM}$-4 (3.75 cm axial FOV), LabPET$^{TM}$-8 (7.5 cm axial FOV) and LabPET$^{TM}$-12 (11.4 cm axial FOV) (Bergeron *et al* 2009b). Following the widespread use and commercial availability of small animal PET scanners, the National Electrical Manufacturers Association (NEMA) published its NU 4–2008 standards (National Electrical Manufacturers Association 2008), a consistent and standardized methodology for measuring scanner performance parameters for small animal PET imaging. This work aims to characterize the performance of the LabPET-8$^{TM}$ subsystem of the Triumph$^{TM}$ preclinical multimodality platform using the NEMA NU 4–2008 standards. This includes measurements

**Table 1.** Summary of the LabPET-8$^{TM}$ technical specifications.

| Parameter | Specification |
|---|---|
| Detector crystal material | Phoswich pair of LYSO and LGSO |
| Crystal dimension | $2.0 \times 2.0 \times 14$ mm$^3$ |
| No. of detector rings | 32 |
| Crystals per ring | 192 |
| Total no. of crystals | 6144 |
| Detector ring inner diameter | 162 mm |
| Transaxial FOV | 100 mm |
| Axial FOV | 75 mm |

of the spatial resolution, scatter fraction, count losses and random coincidence measurements, sensitivity and image-quality characteristics. The overall imaging capabilities of the scanner and its suitability for high-resolution molecular imaging are also demonstrated using dedicated phantom and rodent studies.

## 2. Materials and methods

### *2.1. System description*

The Triumph$^{TM}$ PET/SPECT/CT platform is a state-of-the-art preclinical system dedicated for rodents' imaging. The LabPET-8$^{TM}$ subsystem is designed with quasi-individual crystal readout along with parallel digital architecture to achieve the high performance required for high-resolution small animal imaging. The detector array consists of 6144 crystals arranged in contiguous rings with a ring diameter of 16.2 cm and an axial FOV of 7.5 cm. The scintillation crystals are composed of an assembly of $Lu_{0.4}Gd_{1.6}SiO_5$ (LGSO) and $Lu_{1.9}Y_{0.1}SiO_5$ (LYSO) having dimensions of $2 \times 2 \times 14$ mm$^3$, which are optically coupled one after the other, creating phoswich pairs of detectors. This combination of two different crystal materials is useful for efficient determination of the depth of interaction through crystal identification by digital pulse shaping analysis. Four phoswich detectors are covered in a hermetic container made-up of kovar (an iron–nickel–cobalt alloy with density of 8.359 g cm$^{-3}$) having outer dimensions of $10.3 \times 4.7 \times 18$ mm$^3$. Some important characteristics and features of the LabPET-8$^{TM}$ are summarized in table 1. Additional details about the LabPET-8$^{TM}$ design and architecture are given elsewhere (Tetrault *et al* 2008, Fontaine *et al* 2009).

Unless otherwise stated, all PET studies are acquired using a 250–650 keV energy window and 22 ns coincidence-timing window. The list-mode data were binned into three-dimensional (3D) histograms or sinograms. These 3D sinograms were further rebinned to two-dimensional (2D) sinograms using single-slice rebinning (SSRB). Images were reconstructed using either 2D analytic filtered backprojection or iterative maximum-likelihood expectation maximization (MLEM) algorithms with ten iterations for the latter.

The physical response of the scanner is modeled during iterative reconstruction using an analytic model of the geometrical detector response function (Selivanov *et al* 2000). The shift-varying analytic formulation is based on the linear attenuation of photons in a detector array which is used in the derivation of the system matrix, thus allowing accurate modeling of the relationship between the image representation space and the space of projections. The model was incorporated within a 2D iterative MLEM reconstruction process using precomputed system response coefficients. The physical response of the scanner fully compensates for

the missing data due to in-plane gaps between detector modules. The LabPET-8$^{TM}$ scanner provides the option of image reconstruction in a high-resolution mode using 0.25 mm pixel size instead of 0.5 mm used in the normal mode.

A direct data-based method is used for normalization. This is performed by rotating a 37 MBq of $^{68}$Ga/$^{68}$Ge rod source around the detectors. The acquisition time lasts about 8–10 h depending on rod source activity. The acquired data were not corrected for attenuation or scatter and reconstructed without post-reconstruction smoothing.

### *2.2. Spatial resolution*

The spatial resolution was evaluated using a $^{22}$Na point source having dimensions of 0.25 mm and an activity of 1.11 MBq enclosed in an acrylic cube of 1 cm$^3$ (Eckert & Ziegler Isotope Products, Valencia CA). Data were acquired at the center of the FOV ($Z = 0$ mm) and one-fourth of the axial FOV ($Z = 18.8$ mm) for radial offsets of 5, 10, 15 and 25 mm. Each acquisition had more than $10^5$ prompt counts. The variations in detector efficiency were compensated through normalization using a $Ge^{68}/Ga^{68}$ rod source. The SSRB sorted data were reconstructed using 2D FBP without smoothing. The spatial resolution in radial, tangential and axial directions was analyzed in terms of full width at half-maximum (FWHM) and full width at tenth maximum (FWTM) according to NEMA NU 4–2008 standards. The scanner design is optimized for iterative reconstruction taking advantage of modeling the system response of the scanner to improve the spatial resolution and overall image quality (Selivanov *et al* 2000). The spatial resolution was also calculated using 2D MLEM iterative reconstruction with 40 iterations and span of 5. Both FBP and MLEM reconstructions were performed in a high-resolution mode. The volumetric resolution was computed as the product of the axial, radial and tangential resolutions.

### *2.3. Scatter fraction and counting rate measurements*

Scatter fraction and count rate performance were evaluated using specially designed mouse- and rat-sized phantoms according to NEMA NU 4–2008 specifications. Both phantoms are made-up of a solid, circular cylinder composed of high-density polyethylene (density 0.96 $\pm$ 0.1 g cm$^{-3}$). The mouse-sized phantom is 70 $\pm$ 0.5 mm long and 25 $\pm$ 0.5 mm in diameter whereas the rat-sized phantom has a diameter of 50 $\pm$ 0.5 mm and length of 150 $\pm$ 0.5 mm. A cylindrical hole (3.2 mm diameter) is bored parallel to the central axis at a radial offset of 10 and 17.5 mm for the mouse and rat phantoms, respectively. The starting ($^{18}$F) activity solution is 105 MBq for the mouse-sized phantom and 150 MBq for the rat-sized phantom. Data were acquired after placing the phantoms at the center of the FOV parallel to the *Z*-axis of the scanner. Subsequent acquisitions were recorded until the single-event rate was equal to twice the intrinsic single-event rate. The duration of each acquisition ranged from 180 to 500 s considering the decay of $^{18}$F, thus allowing the collection of more than 500 000 prompt counts. To evaluate the intrinsic scanner counting rate, two acquisitions of 10 h each were performed using the mouse and rat phantoms without any radioactivity. For all acquisitions, prompt sinograms without any corrections were generated. Acquisition and processing of data followed strictly the NEMA NU 4–2008 standards. In short, for each prompt sinogram, all pixels located farther than 8 mm from the edge of the phantom were set to zero. The profile of each projection angle was shifted so that the maximum valued pixels were aligned with the central pixel of the sinogram. After alignment, a sum projection was calculated which resulted in a projection with a peak corresponding to the location of the line source. The average of the pixel values at $\pm$7 mm from the center of the sinogram was multiplied by the number of

pixels between the edges of the 14 mm wide strip. The result was added to the counts outside the strip to provide the total number of scatter and random events. The remaining counts in the sum projection were considered true events and used in the calculation of the true event count rate by dividing with the respective acquisition time. The total number of prompt events in the sinogram, which includes true, scattered and random events, was calculated by summing up all the pixel values in the sum projection.

The true event rate $R_{\text{true}}$ for each acquisition was computed as

$$R_{\text{true}} = \frac{(C_{\text{total}} - C_{\text{random+scatter}})}{T_{\text{acquisition}}}, \tag{1}$$

where $C_{\text{total}}$ is the total number of counts in the sum projection, $C_{\text{random+scatter}}$ is the number of random plus scattered counts and $T_{\text{acquisition}}$ is the total acquisition time.

The scattered event rate $R_{\text{scatter}}$ for each acquisition was computed as

$$\text{R}_{\text{scatter}} = R_{\text{total}} - R_{\text{true}} - R_{\text{random}} - R_{\text{intrinsic}}, \tag{2}$$

where $R_{\text{total}}$ is the total event rate calculated as

$$R_{\text{total}} = \frac{C_{\text{total}}}{T_{\text{acquisition}}}$$

.

The random event rate $R_{\text{random}}$ for each acquisition was computed as

$$R_{\text{random}} = R_{\text{total}} - \left(\frac{R_{\text{true}}}{1 - SF}\right). \tag{3}$$

The scatter fraction for each acquisition was computed using the following formula:

$$\text{SF} = \frac{R_{\text{scatter}}}{R_{\text{true}} + R_{\text{scatter}}}. \tag{4}$$

The noise equivalent count rate (NECR) $R_{\text{NEC}}$ for each acquisition was computed as

$$R_{\text{NEC}} = \frac{R_{\text{true}}^2}{R_{\text{total}}}. \tag{5}$$

The scatter fraction, count losses and random coincidence analysis were implemented using an in-house developed program implemented in MATLAB 7.4 (Mathworks, Natick, MA).

### *2.4. Sensitivity*

The sensitivity was measured using the same $^{22}$Na point source used in the above-described spatial resolution measurements. An acquisition was performed for 10 000 true events by centering the source in the scanner's FOV. The acquisition time was noted and utilized for subsequent acquisitions at positions stepped axially covering the whole scanner's axial FOV. Also, the background true event rate was measured by acquiring data in the absence of a radioactive source in the FOV. All data were analyzed according to NEMA NU 4–2008 standards.

The sensitivity (counts per second per Bq or cps Bq$^{-1}$) was calculated as follows:

$$S_i = \left(\frac{R_i - R_{B,i}}{A_{\text{cal}}}\right), \tag{6}$$

where $R_i$ and $R_{\text{B},i}$ are the source and background count rates for acquisition $i$, respectively, and $A_{\text{cal}}$ is the actual point source activity.

The relative (percent) sensitivity for acquisition $i$ is given by

$$S_{\text{A},i} = \frac{S_i}{0.906} \times 100, \tag{7}$$

where 0.906 is the branching ratio of $^{22}$Na.

The system sensitivity for the mouse and rat phantoms was computed as follows:

$$\mathrm{SM_{tot}} = \sum_{\substack{\text{central}\\ \text{7cm}}} S_i; \quad \mathrm{SR_{tot}} = \sum_{\substack{\text{central}\\ \text{15cm}}} S_i; \quad \mathrm{SM_{A,tot}} = \sum_{\substack{\text{central}\\ \text{7cm}}} S_{A,i}; \quad \mathrm{SR_{A,tot}} = \sum_{\substack{\text{central}\\ \text{15cm}}} S_{A,i}, \tag{8}$$

where central 7 cm and central 15 cm are the central axial FOVs of the scanner encompassing 7 cm and 15 cm of length corresponding to typical length of mouse and rat, respectively.

The total system sensitivity was computed as follows:

$$S_{\mathrm{tot}} = \sum_{\substack{\text{all}\\ i}} S_i; \quad S_{\mathrm{A,tot}} = \sum_{\substack{\text{all}\\ i}} S_{A,i}. \tag{9}$$

The axial sensitivity profile was plotted using the sensitivity, $S_{A,i}$, for each slice.

### *2.5. Image-quality characteristics*

Image-quality characteristics were assessed using a specially designed NEMA NU 4–2008 image-quality phantom. The phantom is made-up of polymethylmethacrylate with internal dimensions of 50 length and 30 mm diameter. The phantom consists of three compartments: a uniform region, five rods of different diameters and two non-radioactive chambers. The phantom was filled with 6.1 MBq of $^{18}$F. The acquisition started when the activity in the phantom was 3.7 MBq and lasted 20 min. Normalization and random corrections were applied to the acquired data before image reconstruction. The PET emission data were reconstructed using 2D-MLEM (10 iterations, span 63) resulting in a 240 × 240 × 63 image matrix with the voxel size of 0.25 × 0.25 × 1.17 mm$^3$. A 22.5 mm diameter (75% of active diameter) × 10 mm depth cylindrical volume of interest (VOI) was drawn over the center of the uniform region of the image-quality phantom. The average activity concentration, maximum and minimum values in the VOI, and the percentage standard deviation (%STD) were measured. The reconstructed image slices covering the central 10 mm length of the rods were averaged to obtain a single slice of lower noise. Circular regions of interest (ROIs) were drawn on this image, around each rod and background, with diameters twice the physical diameter of the rods. The maximum values in each of these ROIs were measured. The transverse image pixel coordinates of the locations with the maximum ROI values were recorded and used to create line profiles along the rods in the axial direction. The standard deviation and mean value of a rod profile and background were calculated. These are referred to as $\mathrm{SD_{line\ profile}}$, $\mathrm{average_{line\ profile}}$, $\mathrm{SD_{background}}$ and $\mathrm{average_{background}}$. Spill-over ratios (SOR) were calculated by drawing VOIs (diameter 4 mm, 7.5 mm in length) on the water- and air-filled cylindrical chambers. The ratio of the mean counts in each cold region to the mean of the hot uniform area was reported as SOR.

The standard deviation of the recovery coefficients (RC) was calculated as follows:

$$SD_{RC} = \sqrt{\left(\frac{\mathrm{SD_{lineprofile}}}{\mathrm{average_{lineprofile}}}\right)^2 + \left(\frac{\mathrm{SD_{background}}}{\mathrm{average_{background}}}\right)^2}. \tag{10}$$

*2.5.1. Imaging study.* To access the overall system performance, the imaging capabilities of the scanner were assessed through additional imaging studies of rodents. A healthy wistar rat was injected intravenously with 30 MBq of [$^{18}$F]-FDG. PET images were acquired 45 min post-injection. The total acquisition time was 19 min for three bed positions. Similar reconstruction procedure was applied for the phantom studies described above.

## 3. Results

### *3.1. Spatial resolution*

The measured radial, tangential and axial spatial resolution in terms of FWHM and FWTM (mm) are plotted in figure 1 for FBP reconstruction as recommended by the NEMA NU 4—2008 standards. The FWHM radial resolution ranged from 1.7 mm at the center of the FOV to 2.59 mm at a radial offset of 25 mm, whereas the FWTM ranged from 3.1 to 4.91 mm for the same radial offset. The axial resolution ranged from 2.41 mm at the center FOV to 2.63 mm at a radial offset of 25 mm, whereas the FWTM ranged from 4.4 to 4.79 mm for the same radial offset. The tangential resolution was more or less constant for the radial offsets. The FWHM volumetric resolutions at axial positions $Z = 0$ and 18.8 mm are 7.5 and 8.3 mm$^3$, respectively.

Figure 2 represents the MLEM reconstructed radial, tangential and axial spatial resolutions in terms of FWHM and FWTM (mm). Iterative reconstruction with accurate statistical modeling of the system's response function improved substantially the spatial resolution. The radial resolution ranged from 0.84 mm at the center of the FOV to 1.14 mm at a radial offset of 25 mm, whereas the FWTM ranged from 1.53 to 2.08 mm for the same radial offset. The axial resolution ranged from 1.55 mm at the center of the FOV to 1.53 mm at a radial offset of 25 mm, whereas the FWTM ranged from 2.83 to 2.81 mm for the same radial offset. The tangential resolution was almost constant for the radial offsets. The FWHM volumetric resolutions at axial positions $Z = 0$ and 18.8 mm positions are 1.31 and 1.43 mm$^3$, respectively.

### *3.2. Scatter fraction, count losses and random coincidence measurements*

The count rate performance of the scanner for the mouse- and rat-sized phantoms is shown in figure 3. The total, true, random, scatter and NEC rates are plotted against the average effective activity concentration for both mouse- and rat-sized phantoms. For the mouse-sized phantom, the peak NECR is 183 kcps at 2.07 MBq cc$^{-1}$, whereas the peak true count rate is 320 kcps at 2.50 MBq cc$^{-1}$ with a scatter fraction of 19%. The rat-sized phantom produced a scatter fraction of 31%, with a peak NECR of 67 kcps at 0.23 MBq cc$^{-1}$ and a peak true count rate of 186 kcps at 0.27 MBq cc$^{-1}$.

### *3.3. Sensitivity*

The NEMA NU 4–2008 standards suggest calculating the system sensitivity as the sum of the sensitivity for each slice. The total sensitivity for the mouse and rat length is 0.16 cps Bq$^{-1}$, whereas the total absolute sensitivity is 12.74%. The system peak absolute sensitivity is 1.33%. Figure 4 depicts the axial sensitivity profile plotted for the absolute sensitivity $S_A$ against each slice.

### *3.4. Image-quality characteristics*

The mean, maximum and minimum activity concentration results and the percentage standard deviation are presented in table 2. The RCs and absolute standard deviation for the different rods are shown in figure 5. The SOR and the %STD obtained for the water- and air-filled inserts of the image-quality phantom are reported in table 3. Representative images of the NEMA image-quality phantom are shown in figure 6, illustrating a transaxial view of the five rods, a coronal view of NEMA image-quality phantom, a transaxial view of the uniform region of the phantom and a profile across the uniform area. The ROI defined for quantitative analysis are also shown.

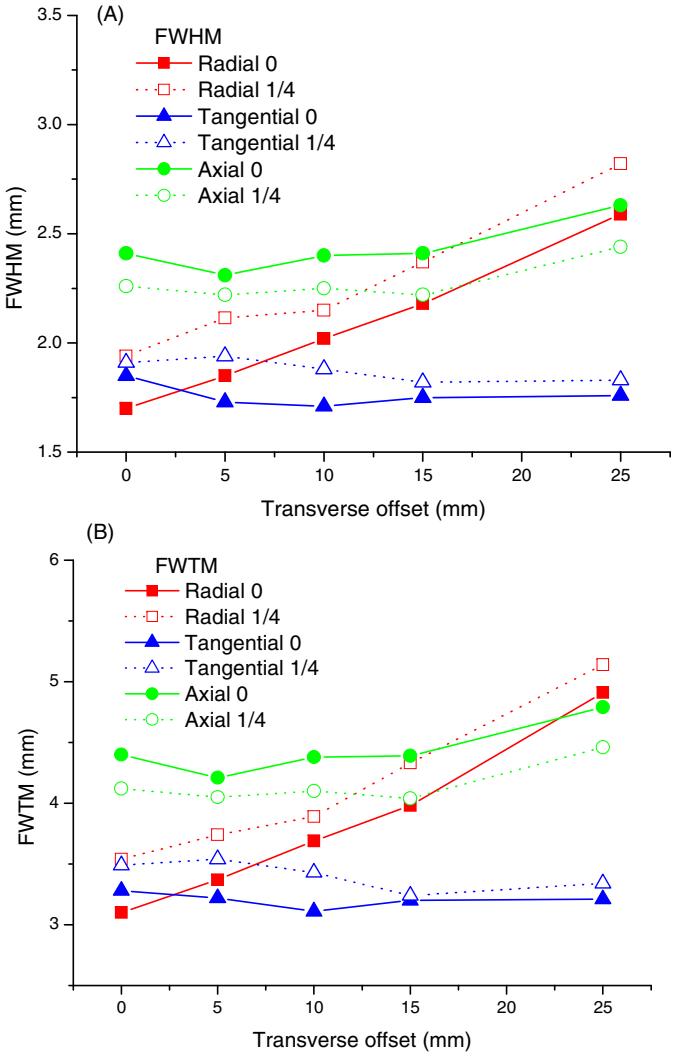


**Figure 1.** Radial, tangential and axial spatial resolution as a function of radial offset reported in terms of FWHM (A) and FWTM (B) using FBP reconstruction. Data were measured at two axial positions: at the center of the axial FOV and at 1/4 from the center of the axial FOV.

**Table 2.** Uniformity analysis results obtained using MLEM reconstructions in terms of mean, maximum and minimum activity concentration values in the defined volume of interest (VOI).

| Mean (kBq ml$^{-1}$) | Maximum (kBq ml$^{-1}$) | Minimum (kBq ml$^{-1}$) | %STD |
|---|---|---|---|
| 126.97 | 156.35 | 97.68 | 7.0% |

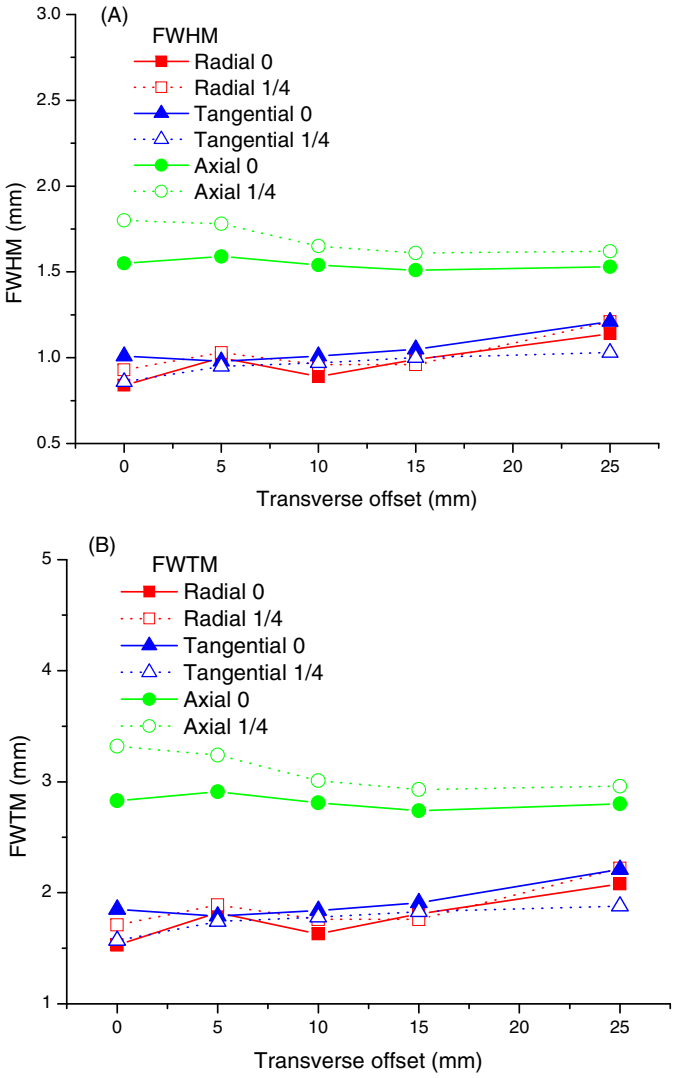


**Figure 2.** Radial, tangential and axial spatial resolution as a function of radial offset reported in terms of FWHM (A) and FWTM (B) using MLEM reconstruction. Data were measured at two axial positions: at the center of the axial FOV and at 1/4 from the center of the axial FOV.

**Table 3.** SOR and standard deviation (%).

| Region | SOR | %STD |
|---|---|---|
| Water-filled cylinder | 0.20 | 16.0 |
| Air-filled cylinder | 0.11 | 9.0 |

### *3.5. Imaging study*

Figure 7 shows transverse, sagittal and coronal views of a wistar rat injected with [$^{18}$F]-FDG acquired to test the PET/CT scanner capabilities for preclinical imaging. The major organs with high uptake of FDG are clearly visible and smaller structures such as the left myocardium

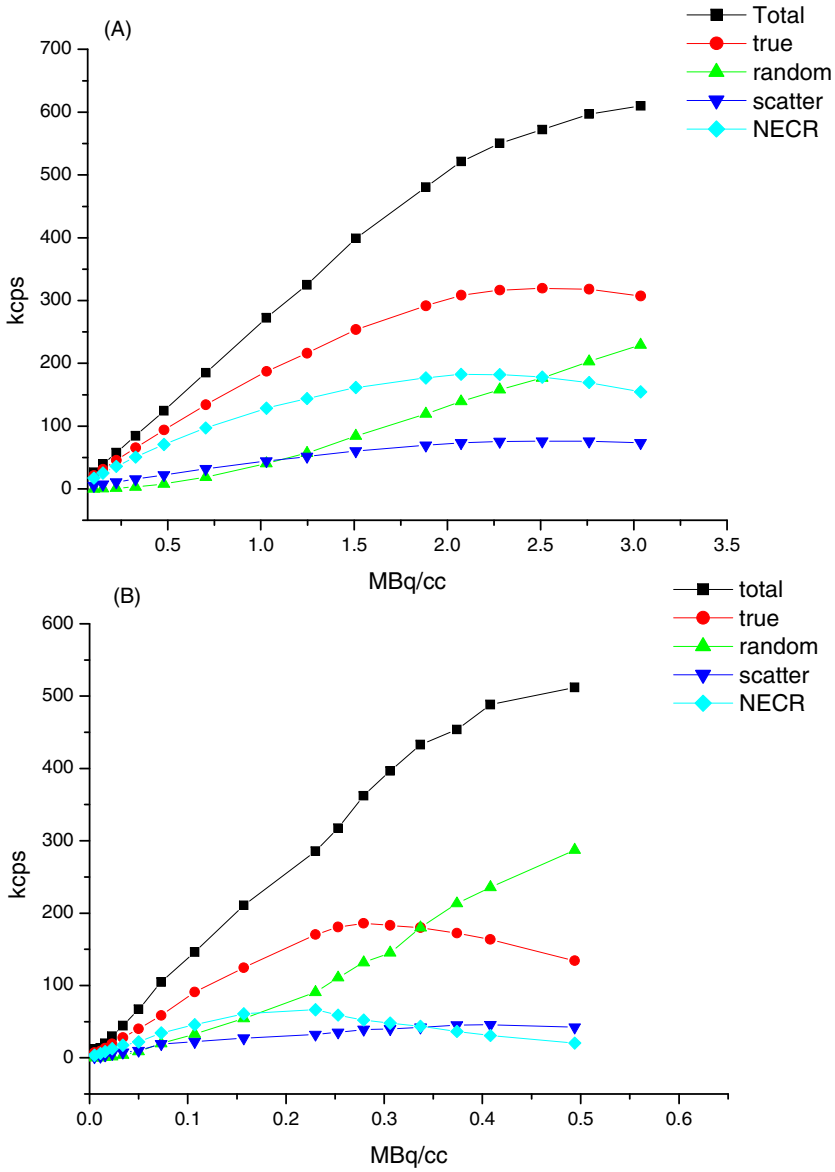


**Figure 3.** Count rate performance plots as a function of the average effective activity concentration of the line source for both a mouse-sized phantom (A) and a rat-sized phantom (B).

and ventricle are clearly defined along the three planes. The much thinner right myocardium is also perceptible on the transaxial slices. The images illustrate the ability of the LabPET-8$^{TM}$ system to obtain good quality and high-contrast images of living rodents and its capabilities to probe subtle molecular signals (low probe concentrations) deep within tissue with high spatial resolution and contrast, and thus provide quantitatively accurate probe spatial and temporal biodistribution data.

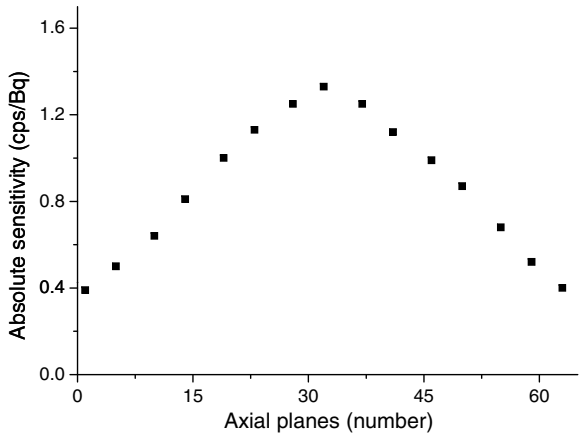


**Figure 4.** The axial absolute sensitivity profile along the $z$-axis of the LabPET-8$^{TM}$ scanner.

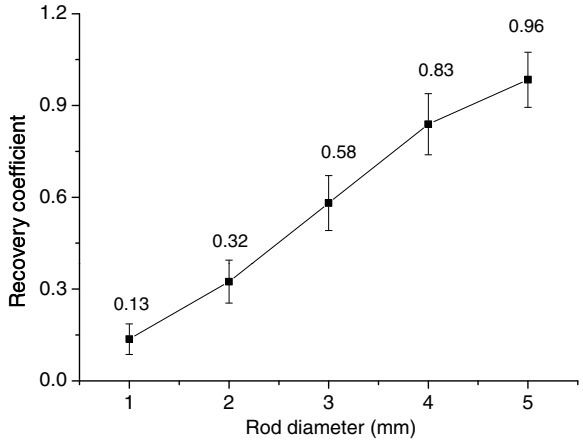


**Figure 5.** Recovery coefficients and standard deviations for five rods of different size ranging between 1 and 5 mm.

## 4. Discussion

The overall performance of the LabPET-8$^{TM}$ subsystem of Triumph$^{TM}$ multimodality platform was evaluated according to NEMA NU 4–2008 standards. Despite the fact that the performance assessment of many small animal PET scanners developed in academic and corporate settings based on the NEMA NU 4–2008 standards is documented in the recent literature (Popota *et al* 2009, Bao *et al* 2009, Lage *et al* 2009, Kis *et al* 2009, Bahri *et al* 2009, Kemp *et al* 2009, Disselhorst *et al* 2010, Prasad *et al* 2010), to the best of our knowledge, there is a lack of the published scientific literature reporting on the performance characterization of the LabPET-8$^{TM}$ system using these standards.

The FBP reconstructed spatial resolution shows that the tangential spatial resolution does not vary significantly throughout the transverse FOV. However, the radial resolution is degraded as the radial offset increases. Despite the two-layer scintillation crystal array or phoswich detector allows the coarse estimation of the photon depth of interaction, there

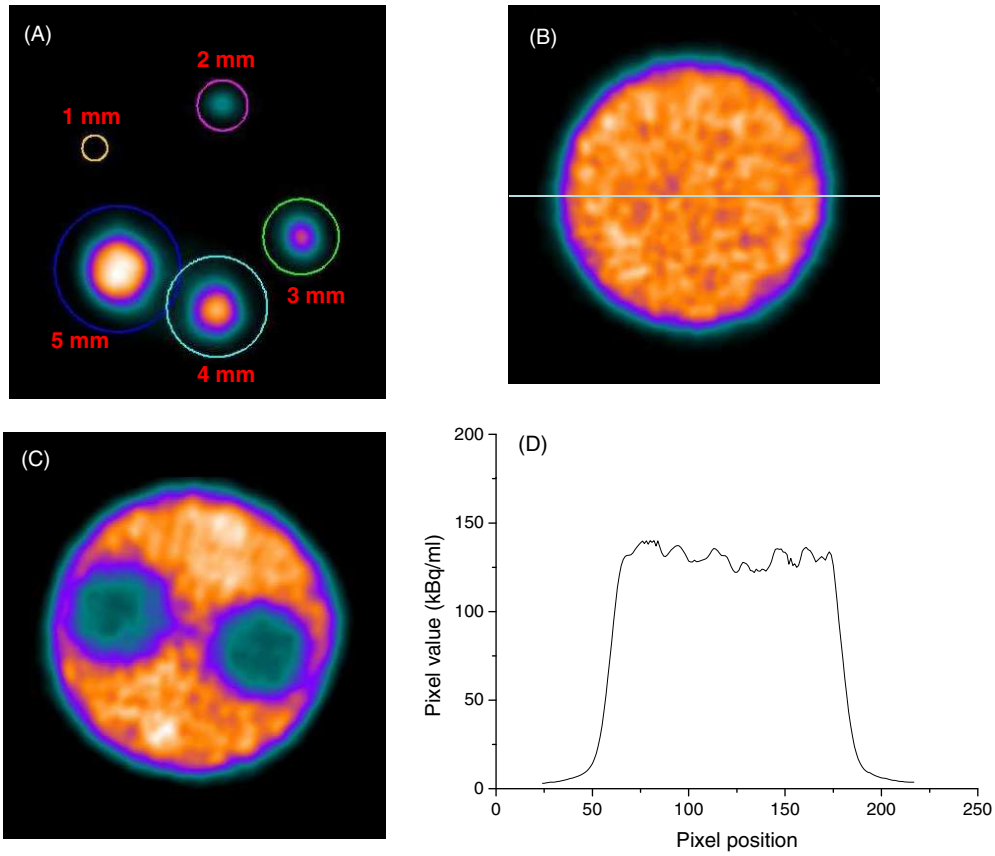


**Figure 6.** Images of the NEMA NU-4 image-quality phantom showing a transverse plane corresponding to the rod region with ROIs defined on each rod (A), a transverse plane of the uniform region (B), a transverse plane of non-radioactive chambers (C), and a line profile across the uniform area of the phantom (D). The defined ROIs for quantitative analysis are also shown.

is a residual transverse parallax error. The deterioration of the axial spatial resolution at higher radial offsets is due to crystal penetration in the axial direction and known limitations of SSRB rebinning used on the LabPET-8$^{TM}$ scanner. In comparison to FBP reconstructed spatial resolution, the MLEM reconstructed spatial resolution, which accurately models the physical response of the scanner in the system matrix, clearly shows the improvement of the spatial resolution in all the three directions. Also, the non-uniformity in the FWHM values of FBP reconstructed spatial resolution has been recovered to a great extent when using MLEM iterative reconstruction and lower span. The spatial resolution results for radial and tangential resolutions are in good agreement with those published for the LabPET$^{TM}$ scanner by the University of Sherbrooke group (Bergeron *et al* 2009a). The slight differences between our and previously published results are due to the difference between acquisition and processing firmware used for generating those results (Tetrault *et al* 2010), difference in the data acquisition energy window (250–650 keV in our case versus 375–650 keV used in the above referenced study) and the maximum ring difference applied (31 in our case versus 15). It should also be noted that we neglected in our calculations the effects of the size and shape of the source and non-collinearity of positron annihilation. Fourier rebinning (FORE) should also replace SSRB to improve the axial spatial resolution of the system.

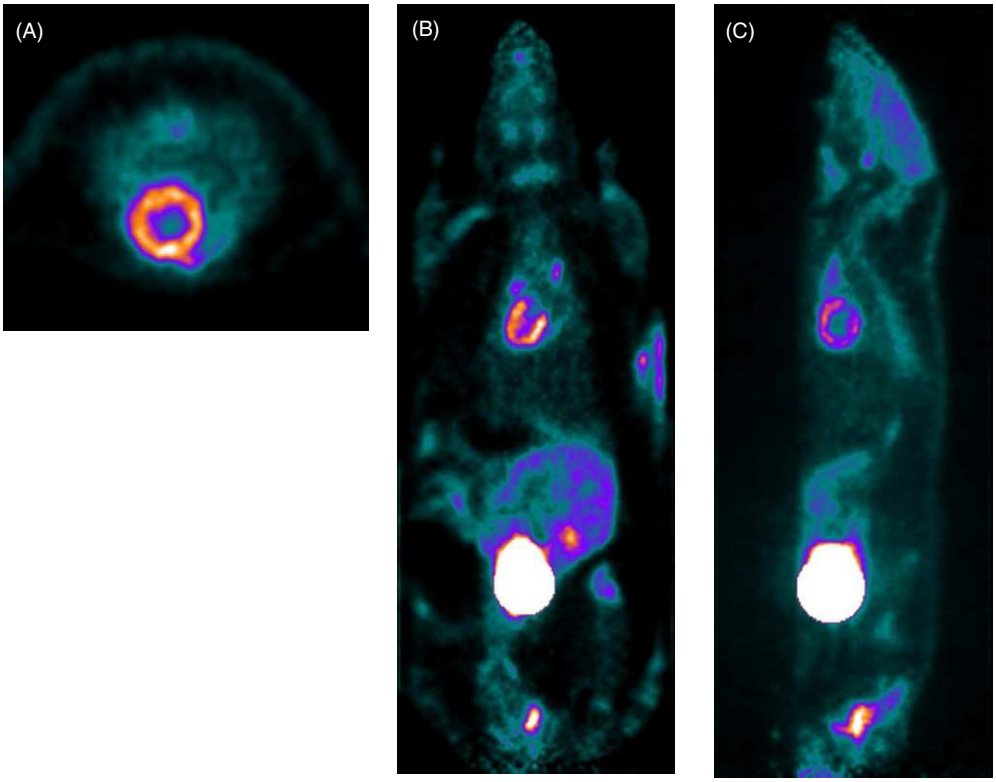


**Figure 7.** Transverse (A), coronal (B) and sagittal (C) representative views of a wistar rat injected with [$^{18}$F]-FDG scanned on the LabPET-8$^{TM}$ scanner.

The measured count rate characteristics demonstrate that the LabPET-8$^{TM}$ has suitable count rate performance for optimal imaging of rodents. The achieved NEMA-based peak NECR of 183 kcps for mouse-sized phantom and of 67 kcps for rat-sized phantom is similar to the results obtained on the eXplore VISTA small animal PET scanner (Wang *et al* 2006). The NECR obtained for the rat-sized phantom is lower than the one obtained for the mouse-sized phantom because of the higher photon attenuation of the true events, and higher scatter and random count rates. The NECR for the mouse-sized phantom peaked at a higher activity concentration than for the rat-sized phantom because the true count rate decreases more rapidly than the random count rate as object size increases (Watson *et al* 2005). The SF values of 19% for the mouse- and 31% for the rat-sized phantoms for the LabPET-8$^{TM}$ scanner are comparable with those reported for the same system (Bergeron *et al* 2008) and for the microPET Focus 120 PET scanner (Kim *et al* 2007).

For an energy window of 250–650 keV and timing window of 22 ns, the system peak absolute sensitivity is 1.33% as compared to 2.1% for the LabPET-8$^{TM}$ scanner (Bergeron *et al* 2009a) using multiple coincidence time windows of 10, 15 and 20 ns for LYSO–LYSO, LGSO–LYSO and LGSO–LGSO. The discrepancy can be due to different time window settings and the noise threshold which is individually applied to each detector to reject the electronic noise. The axial sensitivity profile presents the typical 3D characteristic of axial sensitivities in which a linear drop of sensitivity from the center to the edge of the FOV is observed (figure 4). The NEMA image-quality test provides a common and standardized approach for the overall assessment of image quality of a PET scanner. The %STD which

expresses the uniformity of an image is 7% in contrast to 5.29% reported for the Inveon small animal PET scanner (Bao *et al* 2009). This is due to the fact that our image-quality data are not corrected for attenuation and scatter whereas those of the Inveon scanner are corrected for the above-mentioned physical degrading factors. The recovery coefficients for the five different rods varied from 0.13 to 0.96 (figure 5). These values are similar to those reported earlier for the LabPET$^{TM}$ scanner (Bergeron *et al* 2009a). SOR values of water- and air-filled chambers are 0.20 and 0.11 having %STD of 16% and 9%, respectively. Such high values for SOR were expected since the images were not corrected for attenuation and scatter. The small animal imaging capability of the LabPET-8$^{TM}$ system is also demonstrated by *in vivo* imaging study of a rat injected with [$^{18}$F]-FDG.

Overall, the results demonstrate that the LabPET-8$^{TM}$ subsystem of the Triumph$^{TM}$ multimodality platform is capable of producing high-quality images desirable for molecular imaging-based biomedical research. The performance capabilities of the system can be improved further using fully 3D statistical iterative reconstruction algorithms incorporating accurate modeling of PET scanner response and implementation of CT-based PET quantitative correction procedures.

## 5. Conclusion

The performance of the LabPET-8$^{TM}$ subsystem of the Triumph$^{TM}$ PET/SPECT/CT scanner has been fully characterized using the NEMA NU 04–2008 standards. The results indicate that the scanner has a high and uniform spatial resolution across the FOV and a good sensitivity. The count rate performance results demonstrate that the scanner is well suited for imaging rodents allowing the acquisition of good statistics in a relatively short time. The image-quality phantom results indicate that the image uniformity and RC values are reasonable. However, these performance parameters can be improved by applying appropriate image-correction procedures including CT-based attenuation and scatter corrections (Prasad *et al* 2011, Gutierrez and Zaidi 2011). The overall performance shows that the Triumph$^{TM}$ LabPET-8$^{TM}$ scanner is suitable for preclinical imaging-based research and could be considered as one of the most technologically advanced dedicated small animal PET scanners available today.

## Acknowledgments

This work was supported by the Swiss National Science Foundation under grant SNSF 3152A0-102143. The authors would like to thank Stéphane Germain for his assistance during the planning of the measurements on the Triumph$^{TM}$ system.

## References

Bahri M A, Plenevaux A, Warnock G, Luxen A and Seret A 2009 NEMA NU4-2008 image quality performance report for the microPET Focus 120 and for various transmission and reconstruction methods *J. Nucl. Med.* **50** 1730–8

Bao Q, Newport D, Chen M, Stout D B and Chatziioannou A F 2009 Performance evaluation of the Inveon dedicated PET preclinical tomograph based on the NEMA NU-4 standards *J. Nucl. Med.* **50** 401–8

Bergeron M *et al* 2008 Imaging performance of the LabPET$^{TM}$ APD-based digital PET scanner *IEEE Nuclear Science Symp. Conf. Record* pp 3841–5

Bergeron M *et al* 2009a Performance evaluation of the LabPET APD-based digital PET scanner *IEEE Trans Nucl Sci* **56** 10–6

Bergeron M, Cadorette J, Bureau-Oxton C, Beaudoin J F, Tetrault M A, Leroux J D, Lepage M D, Robert G, Fontaine R and Lecomte R 2009b Performance evaluation of the LabPET12, a large axial FOV APD-based digital PET scanner *IEEE Nuclear Science Symp. Conf. Record (NSS/MIC)* pp 4017–21

Bloomfield P M *et al* 1995 The design and physical characteristics of a small animal positron emission tomograph *Phys. Med. Biol.* **40** 1105–26

Cherry S R, Shao Y, Silverman R W and Meadors K 1997 MicroPET: a high resolution PET scanner for imaging small animals *IEEE Trans. Nucl. Sci.* **44** 1161–6

Del Guerra A, Di Domenico G, Scandola M and Zavattini G 1998 YAP-PET: first results of a small animal positron emission tomograph based on YAP:Ce finger crystals *IEEE Trans. Nucl. Sci.* **45** 3105–8

Disselhorst J A, Brom M, Laverman P, Slump C H, Boerman O C, Oyen W J G, Gotthardt M and Visser E P 2010 Image-quality assessment for several positron emitters using the NEMA NU 4–2008 standards in the Siemens Inveon small-animal PET scanner *J. Nucl. Med.* **51** 610–7

Fontaine R, Belanger F, Viscogliosi N, Semmaoui H, Tetrault M A, Michaud J B, Pepin C, Cadorette J and Lecomte R 2009 The hardware and signal processing architecture of LabPET™, a small animal APD-based digital PET scanner *IEEE Trans. Nucl. Sci.* **56** 3–9

Gutierrez D and Zaidi H 2011 Assessment of scatter for the micro-CT subsystem of the trimodality FLEX triumph preclinical scanner *Med. Phys.* **38** 4154–65

Huisman M C, Reder S, Weber A W, Ziegler S I and Schwaiger M 2007 Performance evaluation of the Philips MOSAIC small animal PET scanner *Eur. J. Nucl. Med. Mol. Imaging* **34** 532–40

Jeavons A P, Chandler R A and Dettmar C A R 1999 A 3D HIDAC-PET camera with sub-millimetre resolution for imaging small animals *IEEE Trans. Nucl. Sci.* **46** 468–73

Kemp B J, Hruska C B, McFarland A R, Lenox M W and Lowe V J 2009 NEMA NU 2–2007 performance measurements of the Siemens Inveon preclinical small animal PET system *Phys. Med. Biol.* **54** 2359–76

Kim J S, Lee J S, Im K C, Kim S J, Kim S-Y, Lee D S and Moon D H 2007 Performance measurement of the microPET Focus 120 scanner *J. Nucl. Med.* **48** 1527–35

Kis S A *et al* 2009 Performance test of the MiniPET-II small animal scanner according to the NEMA NU-4 standards *IEEE Nuclear Science Symp & Medical Imaging Conf.* pp 3185–9

Lage E, Vaquero J J, Sisniega A, Espana S, Tapias G, Abella M, Rodriguez-Ruano A, Ortuno J E, Udias A and Desco M 2009 Design and performance evaluation of a coplanar multimodality scanner for rodent imaging *Phys. Med. Biol.* **54** 5427–41

Lecomte R, Cadorette J, Rodrigue S, Lapointe D, Rouleau D, Bentourkia M, Yao R and Msaki P 1996 Initial results from the Sherbrooke avalanche photodiode positron tomograph *IEEE Trans. Nucl. Sci.* **43** 1952–7

Levin C S and Zaidi H 2007 Current trends in preclinical PET system design *Pet. Clin.* **2** 125–60

National Electrical Manufacturers Association 2008 NEMA standards publication NU 4–2008 *Performance Measurements of Small Animal Positron Emission Tomographs* (Rosslyn, VA: National Electrical Manufacturers Association)

Phelps M E 2000 PET: the merging of biology and imaging into molecular imaging *J. Nucl. Med.* **41** 661–81

Popota F D, Aguiar P, Fernandez Y, Lois C, Pareto D, Ros D, Pavia J and Gispert J D 2009 Comparison of NEMA NU 4-2008 versus NEMA NU 2–2001 for the performance evaluation of the microPET R4 system *IEEE Nuclear Science Symp. & Medical Imaging Conf.* pp 2706–10

Prasad R, Ay M R, Ratib O and Zaidi H 2011 CT-based attenuation correction on the FLEX Triumph™ preclinical PET/CT scanner *IEEE Trans. Nucl. Sci.* **58** 66-75

Prasad R, Ratib O and Zaidi H 2010 Performance evaluation of the FLEX Triumph™ X-PET scanner using the NEMA NU-04 standards *J. Nucl. Med.* **51** 1608–15

Rouze N C, Schmand M, Siegel S and Hutchins G D 2004 Design of a small animal PET imaging system with 1 microliter volume resolution *IEEE Trans. Nucl. Sci.* **51** 757–63

Schafers K P, Reader A J, Kriens M, Knoess C, Schober O and Schafers M 2005 Performance evaluation of the 32-module quadHIDAC small-animal PET scanner *J. Nucl. Med.* **46** 996–1004

Selivanov V V, Picard Y, Cadorette J, Rodrigue S and Lecomte R 2000 Detector response models for statistical iterative image reconstruction in high resolution PET *IEEE Trans. Nucl. Sci.* **47** 1168–75

Stout D B and Zaidi H 2008 Preclinical multimodality imaging *in vivo Pet. Clin.* **3** 251–73

Surti S, Karp J S, Perkins A E, Freifelder R and Muehllehner G 2003 Design evaluation of A-PET: A high sensitivity animal PET camera *IEEE Trans. Nucl. Sci.* **50** 1357–63

Tai Y-C, Chatziioannou A, Yang Y, Silverman R W, Meadors K, Siegel S, Newport D, Stickel J R and Cherry S 2003 MicroPET II: design, development and initial performance of an improved microPET scanner for small-animal imaging *Phys. Med. Biol.* **48** 1519–37

Tai Y C, Ruangma A, Rowland D, Siegel S, Newport D F, Chow P L and Laforest R 2005 Performance evaluation of the microPET focus: a third-generation microPET scanner dedicated to animal imaging *J. Nucl. Med.* **46** 455–63

Tetrault M A, Bergeron M, Lecomte R and Fontaine R 2010 Firmware upgrade for the data acquisition system of the LabPET small animal PET scanner *IEEE Trans. Nucl. Sci.* **57** 556–60

Tetrault M A *et al* 2008 System architecture of the LabPET small animal PET scanner *IEEE Trans. Nucl. Sci.* **55** 2546–50

Wang Y, Seidel J, Tsui B M, Vaquero J J and Pomper M G 2006 Performance evaluation of the GE healthcare eXplore VISTA dual-ring small-animal PET scanner *J. Nucl. Med.* **47** 1891–900

Watson C C, Casey M E, Bendriem B, Carney J P, Townsend D W, Eberl S, Meikle S and Difilippo F P 2005 Optimizing injected dose in clinical PET by accurately modeling the counting-rate response functions specific to individual patient scans *J. Nucl. Med.* **46** 1825–34

Xie S, Ramirez R, Liu Y, Xing T, Uribe J, Li H, Wang Y, Baghaei H, Kim S and Wong W-H 2005 A pentagon photomultiplier-quadrant-sharing BGO detector for a rodent research PET (RRPET) *IEEE Trans. Nucl. Sci.* **52** 210–6

Ziemons K *et al* 2005 The ClearPET$^{TM}$ project: development of a 2nd generation high-performance small animal PET scanner *Nucl. Instrum. Methods* A **537** 307–11